

**JOURNAL OF THE ROYAL SOCIETY
INTERFACE**

Off-axis electron holography of bacterial cells and magnetic nanoparticles in liquid

Journal:	<i>Journal of the Royal Society Interface</i>
Manuscript ID	rsif-2017-0464.R2
Article Type:	Research
Date Submitted by the Author:	n/a
Complete List of Authors:	Prozorov, Tanya; US DOE Ames Laboratory, Division of Materials Sciences Almeida, Trevor; University of Glasgow College of Science and Engineering, University of Glasgow Kovács, András ; Forschungszentrum Julich, Ernst Ruska-Centre for Microscopy and Spectroscopy with Electrons and, Peter Grünberg Institute Dunin-Borkowski, Rafal ; Forschungszentrum Julich, Ernst Ruska-Centre for Microscopy and Spectroscopy with Electrons and, Peter Grünberg Institute
Categories:	Life Sciences - Physics interface
Subject:	Nanotechnology < CROSS-DISCIPLINARY SCIENCES
Keywords:	off-axis electron holography, magnetic nanoparticles, liquid cell TEM, in situ imaging, magnetotactic bacteria

SCHOLARONE™
Manuscripts

1
2
3
4
5
6
7
8
9
10⁴
11
12
13
14
15
16
17
18
19
20
21
22
23
24
25
26
27
28
29
30
31
32
33
34
35
36
37
38
39
40
41
42
43
44
45
46
47
48
49
50
51
52
53
54
55
56
57
58
59
60

Off-axis electron holography of bacterial cells and magnetic nanoparticles in liquid

Tanya Prozorov ^{1*}, Trevor P. Almeida ^{2†}, András Kovács ³ and Rafal E. Dunin-Borkowski, ^{3*}

¹ Division of Materials Sciences and Engineering, Ames Laboratory, Ames IA, 50011, USA

² Department of Earth Science and Engineering, Imperial College London,
South Kensington Campus, London SW7 2AZ, UK

[†]Present address: Department of Physics and Astronomy, University of Glasgow,
Glasgow G12 8QQ, UK

³ Ernst Ruska-Centre for Microscopy and Spectroscopy with Electrons and
Peter Grünberg Institute, Forschungszentrum Jülich, 52425 Jülich, Germany

1 18 Abstract

2 19 The mapping of electrostatic potentials and magnetic fields in liquids using electron holography has
3 20 been considered to be unrealistic. Here, we show that hydrated cells of *Magnetospirillum*
4 21 *magneticum* strain AMB-1 and assemblies of magnetic nanoparticles can be studied using off-axis
5 22 electron holography in a fluid-cell specimen holder within the transmission electron microscope.
6 23 Considering the holographic object and reference wave both pass through liquid, the recorded
7 24 electron holograms show sufficient interference fringe contrast to permit reconstruction of the phase
8 25 shift of the electron wave and mapping of the magnetic induction from bacterial magnetite
9 26 nanocrystals. We assess the challenges of performing *in situ* magnetization reversal experiments
10 27 using a fluid cell specimen holder, discuss approaches for improving spatial resolution and
11 28 specimen stability, and outline future perspectives for studying scientific phenomena, ranging from
12 29 interparticle interactions in liquids and electrical double layers at solid-liquid interfaces to
13 30 biominerization and the mapping of electrostatic potentials associated with protein aggregation
14 31 and folding.

15 32 Keywords

16 33 Off-axis electron holography, liquid cell TEM, magnetic nanoparticles, magnetotactic bacteria

17 21
18 22
19 23
20 24
21 25
22 26
23 27
24 28
25 29
26 30
27 31
28 32
29 33
30 34
31 35
32 36
33 37
34 38
35 39
36 40
37 41
38 42
39 43
40 44
41 45
42 46
43 47
44 48
45 49
46 50
47 51
48 52
49 53
50 54
51 55
52 56
53 57
54 58
55 59
56 60

1
2
3 35
4

Introduction

5 36 The localized study of electromagnetic fields in biological systems has been largely
6 37 unexplored, largely due to a lack of suitable characterization techniques across a wide range of
7 38 length scales. Medical applications include the use of pulsed electric or magnetic fields to treat
8 39 pain relief, musculoskeletal trauma and vascular and endocrine disorders^{1,2}. Electric and magnetic
9 40 fields have been shown to play a significant role at the cellular and subcellular level, for example
10 41 in plasma membranes and actin filaments^{3,4}, as well as in processes such as biominerization,
11 42 magnetotaxis^{5,6} and magnetoreception⁷. A key example is the influence of electric fields on
12 43 protein conformation, which has been described using theoretical models⁸⁻¹⁰ and observed
13 44 experimentally¹¹⁻¹⁴. Charge redistribution and localization in proteins, which can be inferred using
14 45 spectroscopic and computational approaches, is crucial to understanding the dynamics of protein
15 46 self-assembly, aggregation and folding^{3,8,15-18}. The development of an experimental technique that
16 47 is capable of visualizing electromagnetic fields and measuring experimental maps of charge
17 48 density and magnetization in biological organisms in liquids with sub-micron spatial resolution
18 49 would advance many fields of science, from nanotechnology to bioimaging.

19 50 The ability to map electrostatic potentials and magnetic fields on the nanoscale is provided
20 51 by the advanced transmission electron microscope (TEM) technique of off-axis electron
21 52 holography. This method involves the use of an electrostatic biprism to facilitate the overlap of an
22 53 electron wave passed through an electron-transparent specimen with a reference wave that has
23 54 passed through vacuum alone. Analysis of the resulting interference fringe pattern provides access
24 55 to both low and high spatial frequencies of the phase shift of the electron wave that has passed
25 56 through the specimen. The phase shift is, in turn, sensitive to electrostatic potentials and magnetic
26 57 fields within and around the specimen, projected in the electron beam direction. The electrostatic
27 58 contribution to the phase shift includes contributions from both longer-range charge redistribution
28 59 and the electrostatic potentials of the constituent atoms, whose spatial average is referred to as the
29 60 mean inner potential (MIP).

30 61 The phase shift can be represented as a sum of electrostatic and magnetic contributions in
31 62 the form

$$41 63 \quad \varphi(x,y) = \varphi_e + \varphi_m = C_E \int V(x,y,z) dz - C_B \int A_Z(x,y,z) dz, \quad (1)$$

42

43 64 where $C_E = \pi\gamma/\lambda U^*$ is an interaction constant that depends on the accelerating voltage of the
44 65 electron microscope ($C_E = 6.53 \text{ V}^{-1} \mu\text{m}^{-1}$ for 300 kV electrons), λ is the electron wavelength, γ is
45 66 the relativistic Lorentz factor and U^* is the relativistically corrected accelerating potential¹⁹,
46 67 while the constant $C_B = \pi/\phi_0$, where ϕ_0 is the magnetic flux quantum $h/2e = 2.07 \times 10^{-3} \text{ T nm}^2$, is
47 68 independent of the electron energy¹⁹. When examining magnetic fields in materials, the
48 69 electrostatic contribution to the phase is almost always regarded as an unwanted perturbation.
49 70 However, it usually cannot be neglected because of the MIP of the material.

50 71 Off-axis electron holography has primarily been used by physicists and materials
51 72 scientists, with only a small number of reports of the application of the technique to biological
52 73 objects²⁰⁻²². Measurements of the MIP contribution to the phase shift of biological samples using
53 74 off-axis electron holography can in principle be used to study weakly scattering materials,
54 75 providing the possibility to enhance contrast by implementing phase plates in software after

1 76
2 77
3 78
4 79
5 80
6 81
7 82
8 83
9 84
10 85
11 86
12 87
13 88
14 89
15 90
16 91
17 92
18 93
19 94
20 95
21 96
22 97
23 98
24 99
25 100
26 101
27 102
28 103
29 104
30 105
31 106
32 107
33 108
34 109
35 110
36 111
37 112
38 113
39 114
40 115
41 116
42 117
43 118
44 119
45 120
46 121
47 122
48 123
49 124
50 125
51 126
52 127
53 128
54 129
55 130
56 131
57 132
58 133
59 134
60 135
1 136
2 137
3 138
4 139
5 140
6 141
7 142
8 143
9 144
10 145
11 146
12 147
13 148
14 149
15 150
16 151
17 152
18 153
19 154
20 155
21 156
22 157
23 158
24 159
25 160
26 161
27 162
28 163
29 164
30 165
31 166
32 167
33 168
34 169
35 170
36 171
37 172
38 173
39 174
40 175
41 176
42 177
43 178
44 179
45 180
46 181
47 182
48 183
49 184
50 185
51 186
52 187
53 188
54 189
55 190
56 191
57 192
58 193
59 194
60 195
1 196
2 197
3 198
4 199
5 200
6 201
7 202
8 203
9 204
10 205
11 206
12 207
13 208
14 209
15 210
16 211
17 212
18 213
19 214
20 215
21 216
22 217
23 218
24 219
25 220
26 221
27 222
28 223
29 224
30 225
31 226
32 227
33 228
34 229
35 230
36 231
37 232
38 233
39 234
40 235
41 236
42 237
43 238
44 239
45 240
46 241
47 242
48 243
49 244
50 245
51 246
52 247
53 248
54 249
55 250
56 251
57 252
58 253
59 254
60 255
1 256
2 257
3 258
4 259
5 260
6 261
7 262
8 263
9 264
10 265
11 266
12 267
13 268
14 269
15 270
16 271
17 272
18 273
19 274
20 275
21 276
22 277
23 278
24 279
25 280
26 281
27 282
28 283
29 284
30 285
31 286
32 287
33 288
34 289
35 290
36 291
37 292
38 293
39 294
40 295
41 296
42 297
43 298
44 299
45 300
46 301
47 302
48 303
49 304
50 305
51 306
52 307
53 308
54 309
55 310
56 311
57 312
58 313
59 314
60 315
1 316
2 317
3 318
4 319
5 320
6 321
7 322
8 323
9 324
10 325
11 326
12 327
13 328
14 329
15 330
16 331
17 332
18 333
19 334
20 335
21 336
22 337
23 338
24 339
25 340
26 341
27 342
28 343
29 344
30 345
31 346
32 347
33 348
34 349
35 350
36 351
37 352
38 353
39 354
40 355
41 356
42 357
43 358
44 359
45 360
46 361
47 362
48 363
49 364
50 365
51 366
52 367
53 368
54 369
55 370
56 371
57 372
58 373
59 374
60 375
1 376
2 377
3 378
4 379
5 380
6 381
7 382
8 383
9 384
10 385
11 386
12 387
13 388
14 389
15 390
16 391
17 392
18 393
19 394
20 395
21 396
22 397
23 398
24 399
25 400
26 401
27 402
28 403
29 404
30 405
31 406
32 407
33 408
34 409
35 410
36 411
37 412
38 413
39 414
40 415
41 416
42 417
43 418
44 419
45 420
46 421
47 422
48 423
49 424
50 425
51 426
52 427
53 428
54 429
55 430
56 431
57 432
58 433
59 434
60 435
1 436
2 437
3 438
4 439
5 440
6 441
7 442
8 443
9 444
10 445
11 446
12 447
13 448
14 449
15 450
16 451
17 452
18 453
19 454
20 455
21 456
22 457
23 458
24 459
25 460
26 461
27 462
28 463
29 464
30 465
31 466
32 467
33 468
34 469
35 470
36 471
37 472
38 473
39 474
40 475
41 476
42 477
43 478
44 479
45 480
46 481
47 482
48 483
49 484
50 485
51 486
52 487
53 488
54 489
55 490
56 491
57 492
58 493
59 494
60 495
1 496
2 497
3 498
4 499
5 500
6 501
7 502
8 503
9 504
10 505
11 506
12 507
13 508
14 509
15 510
16 511
17 512
18 513
19 514
20 515
21 516
22 517
23 518
24 519
25 520
26 521
27 522
28 523
29 524
30 525
31 526
32 527
33 528
34 529
35 530
36 531
37 532
38 533
39 534
40 535
41 536
42 537
43 538
44 539
45 540
46 541
47 542
48 543
49 544
50 545
51 546
52 547
53 548
54 549
55 550
56 551
57 552
58 553
59 554
60 555
1 556
2 557
3 558
4 559
5 560
6 561
7 562
8 563
9 564
10 565
11 566
12 567
13 568
14 569
15 570
16 571
17 572
18 573
19 574
20 575
21 576
22 577
23 578
24 579
25 580
26 581
27 582
28 583
29 584
30 585
31 586
32 587
33 588
34 589
35 590
36 591
37 592
38 593
39 594
40 595
41 596
42 597
43 598
44 599
45 600
46 601
47 602
48 603
49 604
50 605
51 606
52 607
53 608
54 609
55 610
56 611
57 612
58 613
59 614
60 615
1 616
2 617
3 618
4 619
5 620
6 621
7 622
8 623
9 624
10 625
11 626
12 627
13 628
14 629
15 630
16 631
17 632
18 633
19 634
20 635
21 636
22 637
23 638
24 639
25 640
26 641
27 642
28 643
29 644
30 645
31 646
32 647
33 648
34 649
35 650
36 651
37 652
38 653
39 654
40 655
41 656
42 657
43 658
44 659
45 660
46 661
47 662
48 663
49 664
50 665
51 666
52 667
53 668
54 669
55 670
56 671
57 672
58 673
59 674
60 675
1 676
2 677
3 678
4 679
5 680
6 681
7 682
8 683
9 684
10 685
11 686
12 687
13 688
14 689
15 690
16 691
17 692
18 693
19 694
20 695
21 696
22 697
23 698
24 699
25 700
26 701
27 702
28 703
29 704
30 705
31 706
32 707
33 708
34 709
35 710
36 711
37 712
38 713
39 714
40 715
41 716
42 717
43 718
44 719
45 720
46 721
47 722
48 723
49 724
50 725
51 726
52 727
53 728
54 729
55 730
56 731
57 732
58 733
59 734
60 735
1 736
2 737
3 738
4 739
5 740
6 741
7 742
8 743
9 744
10 745
11 746
12 747
13 748
14 749
15 750
16 751
17 752
18 753
19 754
20 755
21 756
22 757
23 758
24 759
25 760
26 761
27 762
28 763
29 764
30 765
31 766
32 767
33 768
34 769
35 770
36 771
37 772
38 773
39 774
40 775
41 776
42 777
43 778
44 779
45 780
46 781
47 782
48 783
49 784
50 785
51 786
52 787
53 788
54 789
55 790
56 791
57 792
58 793
59 794
60 795
1 796
2 797
3 798
4 799
5 800
6 801
7 802
8 803
9 804
10 805
11 806
12 807
13 808
14 809
15 810
16 811
17 812
18 813
19 814
20 815
21 816
22 817
23 818
24 819
25 820
26 821
27 822
28 823
29 824
30 825
31 826
32 827
33 828
34 829
35 830
36 831
37 832
38 833
39 834
40 835
41 836
42 837
43 838
44 839
45 840
46 841
47 842
48 843
49 844
50 845
51 846
52 847
53 848
54 849
55 850
56 851
57 852
58 853
59 854
60 855
1 856
2 857
3 858
4 859
5 860
6 861
7 862
8 863
9 864
10 865
11 866
12 867
13 868
14 869
15 870
16 871
17 872
18 873
19 874
20 875
21 876
22 877
23 878
24 879
25 880
26 881
27 882
28 883
29 884
30 885
31 886
32 887
33 888
34 889
35 890
36 891
37 892
38 893
39 894
40 895
41 896
42 897
43 898
44 899
45 900
46 901
47 902
48 903
49 904
50 905
51 906
52 907
53 908
54 909
55 910
56 911
57 912
58 913
59 914
60 915
1 916
2 917
3 918
4 919
5 920
6 921
7 922
8 923
9 924
10 925
11 926
12 927
13 928
14 929
15 930
16 931
17 932
18 933
19 934
20 935
21 936
22 937
23 938
24 939
25 940
26 941
27 942
28 943
29 944
30 945
31 946
32 947
33 948
34 949
35 950
36 951
37 952
38 953
39 954
40 955
41 956
42 957
43 958
44 959
45 960
46 961
47 962
48 963
49 964
50 965
51 966
52 967
53 968
54 969
55 970
56 971
57 972
58 973
59 974
60 975
1 976
2 977
3 978
4 979
5 980
6 981
7 982
8 983
9 984
10 985
11 986
12 987
13 988
14 989
15 990
16 991
17 992
18 993
19 994
20 995
21 996
22 997
23 998
24 999
25 1000

1 120 saturation magnetization of magnetite nanoparticles located both within and outside hydrated
2 121 bacterial cells. We also estimate the MIP of the liquid in the fluid cell holder.
3 122
4
5 122
6
7
8 123
9 124
10 125
11 126
12 127
13 128
14 129
15 130
16 131
17 132
18 131
19
20 132
21 133
22 134
23 135
24 136
25 137
26 138
27 139
28 140
29 141
30 142
31 143
32 144
33 145
34 146
35 147
36 148
37 149
38 150
39 151
40 152
41 153
42 154
43 155
44 156
45 157
46 158
47 159
48 160
49 161
50 162
51 163
52 164
53 165
54 166
55 167
56 168
57 169
58 170
59 171
60 172

Results

Figure 1 shows schematic diagrams of the experimental setup for TEM imaging using a fluid cell (**Fig. 1A**) and off-axis electron holography (**Fig. 1B**). Upon assembly of the fluid cell, a small amount of liquid is sandwiched between two electron-transparent SiN membranes. When examining bacterial cells, the microorganisms and surrounding growth medium are trapped by the windows, resulting in a mechanical stress on the bacterial cell walls. In the present study, the holographic reference wave was usually obtained through a layer of liquid, in addition to passing through two 50-nm-thick layers of SiN. The chemical composition of the liquid present, its estimated thickness and the hologram acquisition parameters are given in the Materials and Methods.

Figure 2A shows an off-axis electron hologram of a bacterial specimen in a liquid cell, while **Fig. 2B** shows a corresponding reconstructed (wrapped) phase image. Since the phase shift is dominated by the MIP contribution to the phase, it represents the thickness profile of the specimen in a confined geometry, with the bacterial cell located between the SiN membranes and the liquid present on both sides of it. It should be noted, however, that the phase image contains features arising from the holographic reference wave, which was also acquired from a liquid-containing region of the sample. The reconstructed amplitude image is shown in **Fig. 2C** and is consistent with the presence of an enclosed bacterial cell. **Figures 2D-F** show a region extracted from the off-axis electron holograms of the hydrated bacterial cell recorded in its initial state (**Fig. 2D**), after tilting by $+75^\circ$ and applying a magnetic field in the direction of the electron beam (**Fig. 2E**) and after tilting by -75° and applying a magnetic field of the same magnitude and direction (**Fig. 2F**). The left side of the image changes between **Fig. 2D** and **Fig. 2F** as a result of electron-beam-induced changes to the liquid, which are indicated in the form of a progression of voids, become more pronounced with cumulative exposure time and can be used to verify the presence of liquid. Significantly, the bacterial cell wall does not appear to have ruptured, as evidenced by the bacterial body maintaining its integrity and shape, as well as its relatively constant density during imaging. The cell wall may correspond to the bright band that is visible around the periphery of the cell in the phase image shown in **Fig. 2B**. **Figure 2G** shows a relevant part of a magnetic induction map recorded from the magnetite nanocrystal chain in the bacterial cell. The individual magnetite nanocrystals are outlined in white, while the direction of the projected in-plane magnetic induction is indicated using arrows and colors. For clarity, the phase contours have been obscured on the left side of the image, which contains artifacts associated with the electron-beam-induced bubbling of the liquid. The magnetic induction map in **Fig. 2G**, which was determined from the magnetic contribution to the phase shift reconstructed from the electron holograms shown in **Fig. 2E** and **Fig. 2F**, provides a quantitative representation of the magnetic field in the magnetite nanocrystals, which each contain a single magnetic domain, as well as the stray magnetic field around them. **Fig. 2H** shows a profile of the magnetic contribution to the phase image that was used to create **Fig. 2G**, taken along the red dashed line passing through the center of the crystal, perpendicular to the phase contours. The phase profile was then used to estimate the in-plane magnetic induction across the particle, using a previously described method⁶². To achieve this, the particle was treated as a sphere and the difference between the maximum

1 163
2 164
3 and minimum values of the magnetic contribution to the phase shift were substituted into the
4 equation: $\Delta\phi_{\text{mag}} = 2.044(e/h)B_{\perp}a^2$, where e is the magnitude of electronic charge, \hbar is reduced
5 Planck's constant, a is the particle's radius and B_{\perp} is the in-plane magnetic induction. In the case
6 for spherical particles, the measured B_{\perp} is only 2/3 of the saturated magnetic induction and after
7 including this correction, the latter was estimated as 0.58 ± 0.1 T, which is consistent with the
8 room temperature saturation induction of magnetite⁶².
9

10 169
11 **Figure 3** shows an off-axis electron hologram and a corresponding magnetic induction
12 map recorded from a magnetite nanocrystal chain that had been released from a ruptured
13 bacterium inside the fluid cell. When compared to the hydrated bacterium shown in **Fig. 2**, the
14 Michelson contrast ratio increases from $\sim 15\%$ to $\sim 30\%$ and the spatial resolution is improved,
15 presumably due to the absence of the protoplasm and cellular compartments seen in **Fig. 2**. The
16 magnetic induction map shown in **Fig. 3B** again provides a quantitative representation of the
17 magnetic field in the magnetite grains and their magnetostatic interactions. In a similar fashion to
18 **Fig. 2H**, **Fig. 3C** shows a profile of the magnetic contribution to the phase image, taken along the
19 red dashed line passing through the center of the crystal in **Fig 3B**. A saturated magnetic induction
20 of 0.63 ± 0.1 T was estimated for the particle, which is again consistent with the room temperature
21 saturation induction of magnetite⁶². The blurring of the contour lines in the lower-most crystal in
22 **Fig. 3B** could result from the presence of a magnetic vortex domain state or a crystallographic
23 twin, as seen in **Fig. 3A**⁶¹. These possibilities make the magnetic signal in this crystal difficult to
24 interpret. The large magnetite crystal adjacent to the twinned crystal is surrounded by biological
25 cellular material that is likely to be a remnant membrane and the liquid appears to cover only the
26 left part of the chain.
27
28 182
29 183
30 184
31 185
32 186
33 187
34 188
35 189
36 190
37 191
38 192
39 193
40 194
41 195
42 196
43 197
44 198
45 199
46 200
47 201
48 202
49 203
50 204
51 205
52 206
53 207
54 208
55 209
56 210
57 211
58 212
59 213
60 214

30 185
31 186
32 187
33 188
34 189
35 190
36 191
37 192
38 193
39 194
40 195
41 196
42 197
43 198
44 199
45 200
46 201
47 202
48 203
49 204
50 205
51 206
52 207
53 208
54 209
55 210
56 211
57 212
58 213
59 214
60 215
30 185
31 186
32 187
33 188
34 189
35 190
36 191
37 192
38 193
39 194
40 195
41 196
42 197
43 198
44 199
45 200
46 201
47 202
48 203
49 204
50 205
51 206
52 207
53 208
54 209
55 210
56 211
57 212
58 213
59 214
60 215
30 185
31 186
32 187
33 188
34 189
35 190
36 191
37 192
38 193
39 194
40 195
41 196
42 197
43 198
44 199
45 200
46 201
47 202
48 203
49 204
50 205
51 206
52 207
53 208
54 209
55 210
56 211
57 212
58 213
59 214
60 215
30 185
31 186
32 187
33 188
34 189
35 190
36 191
37 192
38 193
39 194
40 195
41 196
42 197
43 198
44 199
45 200
46 201
47 202
48 203
49 204
50 205
51 206
52 207
53 208
54 209
55 210
56 211
57 212
58 213
59 214
60 215
30 185
31 186
32 187
33 188
34 189
35 190
36 191
37 192
38 193
39 194
40 195
41 196
42 197
43 198
44 199
45 200
46 201
47 202
48 203
49 204
50 205
51 206
52 207
53 208
54 209
55 210
56 211
57 212
58 213
59 214
60 215
30 185
31 186
32 187
33 188
34 189
35 190
36 191
37 192
38 193
39 194
40 195
41 196
42 197
43 198
44 199
45 200
46 201
47 202
48 203
49 204
50 205
51 206
52 207
53 208
54 209
55 210
56 211
57 212
58 213
59 214
60 215
30 185
31 186
32 187
33 188
34 189
35 190
36 191
37 192
38 193
39 194
40 195
41 196
42 197
43 198
44 199
45 200
46 201
47 202
48 203
49 204
50 205
51 206
52 207
53 208
54 209
55 210
56 211
57 212
58 213
59 214
60 215
30 185
31 186
32 187
33 188
34 189
35 190
36 191
37 192
38 193
39 194
40 195
41 196
42 197
43 198
44 199
45 200
46 201
47 202
48 203
49 204
50 205
51 206
52 207
53 208
54 209
55 210
56 211
57 212
58 213
59 214
60 215
30 185
31 186
32 187
33 188
34 189
35 190
36 191
37 192
38 193
39 194
40 195
41 196
42 197
43 198
44 199
45 200
46 201
47 202
48 203
49 204
50 205
51 206
52 207
53 208
54 209
55 210
56 211
57 212
58 213
59 214
60 215
30 185
31 186
32 187
33 188
34 189
35 190
36 191
37 192
38 193
39 194
40 195
41 196
42 197
43 198
44 199
45 200
46 201
47 202
48 203
49 204
50 205
51 206
52 207
53 208
54 209
55 210
56 211
57 212
58 213
59 214
60 215
30 185
31 186
32 187
33 188
34 189
35 190
36 191
37 192
38 193
39 194
40 195
41 196
42 197
43 198
44 199
45 200
46 201
47 202
48 203
49 204
50 205
51 206
52 207
53 208
54 209
55 210
56 211
57 212
58 213
59 214
60 215
30 185
31 186
32 187
33 188
34 189
35 190
36 191
37 192
38 193
39 194
40 195
41 196
42 197
43 198
44 199
45 200
46 201
47 202
48 203
49 204
50 205
51 206
52 207
53 208
54 209
55 210
56 211
57 212
58 213
59 214
60 215
30 185
31 186
32 187
33 188
34 189
35 190
36 191
37 192
38 193
39 194
40 195
41 196
42 197
43 198
44 199
45 200
46 201
47 202
48 203
49 204
50 205
51 206
52 207
53 208
54 209
55 210
56 211
57 212
58 213
59 214
60 215
30 185
31 186
32 187
33 188
34 189
35 190
36 191
37 192
38 193
39 194
40 195
41 196
42 197
43 198
44 199
45 200
46 201
47 202
48 203
49 204
50 205
51 206
52 207
53 208
54 209
55 210
56 211
57 212
58 213
59 214
60 215
30 185
31 186
32 187
33 188
34 189
35 190
36 191
37 192
38 193
39 194
40 195
41 196
42 197
43 198
44 199
45 200
46 201
47 202
48 203
49 204
50 205
51 206
52 207
53 208
54 209
55 210
56 211
57 212
58 213
59 214
60 215
30 185
31 186
32 187
33 188
34 189
35 190
36 191
37 192
38 193
39 194
40 195
41 196
42 197
43 198
44 199
45 200
46 201
47 202
48 203
49 204
50 205
51 206
52 207
53 208
54 209
55 210
56 211
57 212
58 213
59 214
60 215
30 185
31 186
32 187
33 188
34 189
35 190
36 191
37 192
38 193
39 194
40 195
41 196
42 197
43 198
44 199
45 200
46 201
47 202
48 203
49 204
50 205
51 206
52 207
53 208
54 209
55 210
56 211
57 212
58 213
59 214
60 215
30 185
31 186
32 187
33 188
34 189
35 190
36 191
37 192
38 193
39 194
40 195
41 196
42 197
43 198
44 199
45 200
46 201
47 202
48 203
49 204
50 205
51 206
52 207
53 208
54 209
55 210
56 211
57 212
58 213
59 214
60 215
30 185
31 186
32 187
33 188
34 189
35 190
36 191
37 192
38 193
39 194
40 195
41 196
42 197
43 198
44 199
45 200
46 201
47 202
48 203
49 204
50 205
51 206
52 207
53 208
54 209
55 210
56 211
57 212
58 213
59 214
60 215
30 185
31 186
32 187
33 188
34 189
35 190
36 191
37 192
38 193
39 194
40 195
41 196
42 197
43 198
44 199
45 200
46 201
47 202
48 203
49 204
50 205
51 206
52 207
53 208
54 209
55 210
56 211
57 212
58 213
59 214
60 215
30 185
31 186
32 187
33 188
34 189
35 190
36 191
37 192
38 193
39 194
40 195
41 196
42 197
43 198
44 199
45 200
46 201
47 202
48 203
49 204
50 205
51 206
52 207
53 208
54 209
55 210
56 211
57 212
58 213
59 214
60 215
30 185
31 186
32 187
33 188
34 189
35 190
36 191
37 192
38 193
39 194
40 195
41 196
42 197
43 198
44 199
45 200
46 201
47 202
48 203
49 204
50 205
51 206
52 207
53 208
54 209
55 210
56 211
57 212
58 213
59 214
60 215
30 185
31 186
32 187
33 188
34 189
35 190
36 191
37 192
38 193
39 194
40 195
41 196
42 197
43 198
44 199
45 200
46 201
47 202
48 203
49 204
50 205
51 206
52 207
53 208
54 209
55 210
56 211
57 212
58 213
59 214
60 215
30 185
31 186
32 187
33 188
34 189
35 190
36 191
37 192
38 193
39 194
40 195
41 196
42 197
43 198
44 199
45 200
46 201
47 202
48 203
49 204
50 205
51 206
52 207
53 208
54 209
55 210
56 211
57 212
58 213
59 214
60 215
30 185
31 186
32 187
33 188
34 189
35 190
36 191
37 192
38 193
39 194
40 195
41 196
42 197
43 198
44 199
45 200
46 201
47 202
48 203
49 204
50 205
51 206
52 207
53 208
54 209
55 210
56 211
57 212
58 213
59 214
60 215
30 185
31 186
32 187
33 188
34 189
35 190
36 191
37 192
38 193
39 194
40 195
41 196
42 197
43 198
44 199
45 200
46 201
47 202
48 203
49 204
50 205
51 206
52 207
53 208
54 209
55 210
56 211
57 212
58 213
59 214
60 215
30 185
31 186
32 187
33 188
34 189
35 190
36 191
37 192
38 193
39 194
40 195
41 196
42 197
43 198
44 199
45 200
46 201
47 202
48 203
49 204
50 205
51 206
52 207
53 208
54 209
55 210
56 211
57 212
58 213
59 214
60 215
30 185
31 186
32 187
33 188
34 189
35 190
36 191
37 192
38 193
39 194
40 195
41 196
42 197
43 198
44 199
45 200
46 201
47 202
48 203
49 204
50 205
51 206
52 207
53 208
54 209
55 210
56 211
57 212
58 213
59 214
60 215
30 185
31 186
32 187
33 188
34 189
35 190
36 191
37 192
38 193
39 194
40 195
41 196
42 197
43 198
44 199
45 200
46 201
47 202
48 203
49 204
50 205
51 206
52 207
53 208
54 209
55 210
56 211
57 212
58 213
59 214
60 215
30 185
31 186
32 187
33 188
34 189
35 190
36 191
37 192
38 193
39 194
40 195
41 196
42 197
43 198
44 199
45 200
46 201
47 202
48 203
49 204
50 205
51 206
52 207
53 208
54 209
55 210
56 211
57 212
58 213
59 214
60 215
30 185
31 186
32 187
33 188
34 189
35 190
36 191
37 192
38 193
39 194
40 195
41 196
42 197
43 198
44 199
45 200
46 201
47 202
48 203
49 204
50 205
51 206
52 207
53 208
54 209
55 210
56 211
57 212
58 213
59 214
60 215
30 185
31 186
32 187
33 188
34 189
35 190
36 191
37 192
38 193
39 194
40 195
41 196
42 197
43 198
44 199
45 200
46 201
47 202
48 203
49 204
50 205
51 206
52 207
53 208
54 209
55 210
56 211
57 212
58 213
59 214
60 215
30 185
31 186
32 187
33 188
34 189
35 190
36 191
37 192
38 193
39 194
40 195
41 196
42 197
43 198
44 199
45 200
46 201
47 202
48 203
49 204
50 205
51 206
52 207
53 208
54 209
55 210
56 211
57 212
58 213
59 214
60 215
30 185
31 186
32 187
33 188
34 189
35 190
36 191
37 192
38 193
39 194
40 195
41 196
42 197
43 198
44 199
45 200
46 201
47 202
48 203
49 204
50 205
51 206
52 207
53 208
54 209
55 210
56 211
57 212
58 213
59 214
60 215
30 185
31 186
32 187
33 188
34 189
35 190
36 191
37 192
38 193
39 194
40 195
41 196
42 197
43 198
44 199
45 200
46 201
47 202
48 203
49 204
50 205
51 206
52 207
53 208
54 209
55 210
56 211
57 212
58 213
59 214
60 215
30 185
31 186
32 187
33 188
34 189
35 190
36 191
37 192
38 193
39 194
40 195
41 196
42 197
43 198
44 199
45 200
46 201
47 202
48 203
49 204
50 205
51 206
52 207
53 208
54 209
55 210
56 211
57 212
58 213
59 214
60 215
30 185
31 186
32 187
33 188
34 189
35 190
36 191
37 192
38 193
39 194
40 195
41 196
42 197
43 198
44 199
45 200
46 201
47 202
48 203
49 204
50 205
51 206
52 207
53 208
54 209
55 210
56 211
57 212
58 213
59 214
60 215
30 185
31 186
32 187
33 188
34 189
35 190
36 191
37 192
38 193
39 194
40 195
41 196
42 197
43 198
44 199
45 200
46 201
47 202
48 203
49 204
50 205
51 206
52 207
53 208
54 209
55 210
56 211
57 212
58 213
59 214
60 215
30 185
31 186
32 187
33 188
34 189
35 190
36 191
37 192
38 193
39 194
40 195
41 196
42 197
43 198
44 199
45 200
46 201
47 202
48 203
49 204
50 205
51 206
52 207
53 208
54 209
55 210
56 211
57 212
58 213
59 214
60 215
30 185
31 186
32 187
33 188
34 189
35 190
36 191
37 192
38 193
39 194
40 195
41 196
42 197
43 198
44 199
45 200
46 201
47 202
48 203
49 204
50 205
51 206
52 207
53 208
54 209
55 210
56 211
57 212
58 213
59 214
60 215
30 185
31 186
32 187
33 188
34 189
35 190
36 191
37 192
38 193
39 194
40 195
41 196
42 197
43 198
44 199
45 200
46 201
47 202
48 203
49 204
50 205
51 206
52 207
53 208
54 209
55 210
56 211
57 212
58 213
59 214
60 215
30 185
31 186
32 187
33 188
34 189
35 190
36 191
37 192
38 193
39 194
40 195
41 196
42 197<br

1 Discussion

2

3

4 A significant challenge associated with the use of off-axis electron holography in
5 combination with a fluid cell is the acquisition of a reference electron wave through liquid instead
6 of vacuum. It is also challenging to obtaining a reference electron hologram from an area that is
7 close to the region of interest. In our experiments, the reference hologram was typically acquired
8 from the aqueous medium in a suitable area of the fluid cell that was absent of cell debris. Rapid
9 movement of the liquid front is often reported to have been followed by the formation of voids,
10 vapor-filled bubbles and residual hydrated islands on SiN membranes⁶³⁻⁶⁵. Due to the relatively
11 large size of the bacteria, bright-field imaging of entire cells was typically carried out at low
12 magnification (7000 – 15000 \times)^{5,54,66-68}. Off-axis electron holograms were recorded at higher
13 magnification using a reduced electron dose rate compared to that used for bright-field imaging,
14 requiring longer acquisition times. Bacterial cells were most easily detectable near to the corner or
15 the edge of the SiN window, where the liquid layer was thinnest because the bulging of the SiN
16 membrane is less pronounced in these parts of the cell, resulting in the highest relative signal-to-
17 noise ratio.

18

19

20

21

22 Cells of *Magnetospirillum magneticum*, strain AMB-1, are helical in shape and typically 1-
23 3 μ m in length and 400-600 nm in diameter, with the magnetite nanocrystal chains inside the
24 cytoplasmic membrane and held together by actin-like filaments⁶⁹. Based on our previous
25 experiments on magnetotactic bacteria in a fluid cell using scanning TEM, the liquid layer
26 thickness was typically 500–750 nm at the edges and corners of the SiN windows for the used
27 spacer configuration instead of the nominal thickness of 200 nm, with the magnetite chains acting
28 as natural high-contrast labels denoting the positions of the individual cells of *M. magneticum* (see
29 Experimental Details)⁵¹. Furthermore, the arrangement of the magnetite nanocrystals in chains
30 was indicative that the cell membrane and vesicles had remained intact⁵.

31

32

33

34 In the present experiment, the alignment of the magnetite nanocrystals in chains served an
35 indicator of the integrity of the bacterial cellular structure, as shown in **Fig. 2**. Despite electron-
36 beam-induced displacement and partial evaporation of the liquid surrounding the bacterial cells,
37 we observed no signs of cell wall rupture or release of the magnetite chains, suggesting that the
38 bacteria remained in a hydrated state. However, continuous imaging at high magnification in other
39 regions resulted in damage, as evidenced by the collapse of internal cellular structures, rupture of
40 bacterial cell wall membranes and the release of magnetite nanocrystal chains into the surrounding
41 liquid, followed by amorphization of individual magnetite nanocrystals (**Fig. S1**). When compared
42 to images obtained from dried specimens, the distance between individual magnetite nanocrystals
43 in the fluid cell was observed to have increased slightly^{54,70-72}. This result is consistent with
44 images obtained using cryo-EM^{66,73} and can be attributed to the magnetosome membranes and
45 other sub-cellular compartments remaining in a hydrated state, without the distortions that are
46 typically introduced by the drying of biological matter.

47

48

49

50

51

52

53 Initial magnetic states and magnetization reversal in the fluid cell

54 After magnetizing the hydrated sample in opposite directions *in situ* in the electron
55 microscope and recording electron holograms of oppositely magnetized regions of the same
56 magnetite nanocrystals, the resulting phase images were subtracted from each other to eliminate
57 the contribution of the MIP and hence isolate the magnetic contribution to the phase shift. In such
58 an experiment, the MIP contribution to the phase must be identical in each pair of electron
59

1 250
2 251
3 252
4 253
5 254
6 255
7 256
8 257
9 258
10 259
11 260
12 261
13 262
14 263
15 264
16 265
17 266
18 267
19 268
20 269
21 270
22 271
23 272
24 273
25 274
26 275
27 276
28 277
29 278
30 279
31 280
32 281
33 282
34 283
35 284
36 285
37 286
38 287
39 288
40 289
41 290
42 291
43 292
44 293
45 294
46 295
47 296
48 297
49 298
50 299
51 300
52 301
53 302
54 303
55 304
56 305
57 306
58 307
59 308
60 309
holograms. However, prolonged exposure to the electron beam resulted in evaporation of liquid, void formation and evolution, resulting in the presence of artefacts after calculating differences between each phase image associated with the specimen being magnetized in opposing directions. In the present study, the artifacts associated with the displacement of liquid and void evolution had no apparent effect on the recorded magnetic signal in the magnetite nanocrystals and the magnetic induction map shown in **Fig. 2G** is in good agreement with previous reports of electron holographic imaging of dried bacterial specimens, with the exception of a somewhat larger distance between individual magnetite nanocrystals, which we attribute to the bacterial cell and its subcellular components remaining in a hydrated state^{21,54-56,74,75}. The continuous displacement of liquid in the left part of the image can be used to gauge the residual presence of liquid in the fluid cell, whilst the bacterial cell wall does not appear to have ruptured during imaging, leaving the bacterium hydrated. For comparison, lysed bacterial cells displayed collapsed chains and shorter fragments of magnetite chain, as shown in **Fig. 3**. Although the signal-to-noise ratio is somewhat improved in the fragmented chains when compared to that recorded from an intact bacterial cell (**Fig. 2 D-F**), the magnetic induction map is consistent with that shown in **Fig. 2G**.

21 265
22 266
23 267
24 268
25 269
26 270
27 271
28 272
29 273
30 274
31 275
32 276
33 277
34 278
35 279
36 280
37 281
38 282
39 283
40 284
41 285
42 286
43 287
44 288
45 289
46 290
47 291
48 292
49 293
50 294
51 295
52 296
53 297
54 298
55 299
56 300
57 301
58 302
59 303
60 304
Despite beam-induced displacement and bubbling of the liquid, we recorded off-axis electron holograms with well-resolved interference fringes from different regions of the fluid cell, as shown in **Fig. 4**. We could then reconstruct phase images, such as that shown for a droplet in **Figs 4C-F**, even in the presence of two layers of SiN encasing the liquid in the fluid cell. Similar phase images could be used in future studies of the formation of electrical double layers at solid-liquid interfaces. From the phase image, we estimated the MIP of the liquid at 3.5 ± 0.5 V based on the assumption of a droplet height of ~ 800 nm, in agreement with a value predicted theoretically by Kathmann and co-workers⁷⁶⁻⁷⁹ for the liquid-vapor interface of water, as well as with that measured experimentally for vitrified ice⁸⁰.

Electron-beam-induced damage

35 275
36 276
37 277
38 278
39 279
40 280
41 281
42 282
43 283
44 284
45 285
46 286
47 287
48 288
49 289
50 290
51 291
52 292
53 293
54 294
55 295
56 296
57 297
58 298
59 299
60 300
Whereas the use of a cumulative electron dose on the order of ~ 0.1 e/ \AA^2 has been shown to induce only small changes in cellular structure during a single scanning TEM exposure⁵¹, the imaging conditions for off-axis electron holography typically require a higher electron dose. It has long been postulated that the ultimate resolution for biological materials will be determined by the tolerable electron dose on the specimen^{24,81} and hence that mitigating radiation damage is critical for fluid cell TEM imaging, which has been shown to suffer from electron-beam-induced artifacts⁶³⁻⁶⁵. Although electron beam damage in liquids poses a serious challenge, our results demonstrate that off-axis electron holography in a fluid cell is feasible. In a separate experiment, we imaged using spot size 4 in an attempt to reduce electron beam damage to bacterial cells. This led to a decrease in the overall contrast. However, the interference fringe contrast remained sufficient for data analysis. Several bacterial cells appeared intact and showed no indications of electron beam damage (**Fig. S3**). In the future, direct detection cameras promise to allow image acquisition using shorter exposure times, thereby lowering electron beam damage to both the liquid and the hydrated specimen, as demonstrated in **Figure 5**. More systematic studies aimed at establishing the tolerable electron dose utilized in electron holographic imaging of specimens in liquid will be required. In this regard, the future use of less electron beam sensitive liquids will be beneficial.

1 2 292 3 4 293 5 294 6 295 7 8 296 9 297 10 298 11 299 12 300 13 301 14 302 15 16 303 17 304 18 305 19 306 20 307 21 22 308 23 309 24 310 25 311 26 312 27 313 28 314 29 315 30 316 31 317 32 318 33 319 34 320 35 321 36 322 37 323 38 324 39 325 40 326 41 327 42 328 43 329 44 330 45 331 46 332 47 333 48 334 49 335 50 336 51 337 52 338 53 339 54 340 55 341 56 342 57 343 58 344 59 60 Conclusions

We have demonstrated that off-axis electron holography can be carried out in a commercially available fluid cell TEM specimen holder through a study of hydrated bacterial cells of *M. magneticum* strain AMB-1 in a ~800-nm-thick layer of liquid. Although the liquid surrounding the bacterial cells exhibited signs of electron-beam-induced changes, which contributed to artefacts and noise, the recorded electron holograms showed sufficient interference fringe contrast to permit reconstruction of the phase shift of the electron wave and mapping of the magnetic induction of the bacterial magnetite nanocrystals. We also estimated the mean inner potential of a droplet of liquid at 3.5 ± 0.5 V, based on the assumption that the droplet height was ~800 nm.

Although the choice of liquid and the protocols for data acquisition and processing will need to be refined in the future, in the present study magnetic induction mapping of intracellular magnetite nanocrystals and shorter magnetite chain fragments in liquid was successful. We expect that this approach will be applicable to a wide variety of liquid specimens that contain nanoparticles in their native environment, free of the artefacts that are associated with common preparatory methods.

Off-axis electron holography in liquid offers great promise for studying interactions between magnetic nanoparticles, as well as for the visualization of nanoparticle response to external magnetic stimuli with nanometer spatial resolution. Prospects for other applications of *in situ* off-axis electron holography in a liquid cell include research into magnetic resonance imaging, tissue repair and targeted drug delivery. The method also promises to be applicable to other interfacial phenomena in liquids, including the direct imaging of electrochemical double layers at solid-liquid interfaces, which is of relevance to colloidal suspensions, catalysis, nanofluidic devices, batteries and tribology. Other potential applications include studies of biomineralization and the mapping of electrostatic potentials associated with protein aggregation and folding. The technique promises to open a new era in the physics of liquids by revealing what role magnetostatic and electrostatic interactions play in phase transformations, the physics of coalescence, the effects of confinement and other complex phenomena.

42 320 43 44 Materials and Methods

Fluid cell assembly: Aqueous solutions were prepared using deionized water passed through a Millipore Milli-Q Plus water purification system ($\rho = 18.2$ M Ω cm). *In situ* liquid cell (S)TEM experiments were carried out using a commercial fluid cell holder platform (Hummingbird Scientific, Lacey, WA, USA). The experimental setup consists of a microfluidic chamber, which takes the form of two Si chips with electron-transparent SiN windows in a hermetically-sealed TEM specimen holder⁸⁹. Unless noted otherwise, the SiN chips were plasma-cleaned for 5 minutes prior to use to hydrophilize the surfaces and ensure contaminant removal. A thin liquid layer (typically 200-800 nm thick) was formed by sandwiching two SiN-coated Si chips with a 50×200 μ m electron-transparent 50-nm-thick SiN opening etched from the center, thereby forming an imaging window. Both SiN windows had a 100 nm SU-8 spacer. We drop-casted 1 μ L of liquid onto the top SiN window, removed the excess liquid using filter paper and topped it with the second chip to form the liquid layer. The fluid cell was hermetically sealed to prevent evaporation

1 333
2 334
3 335
4 336
5 337
6 338
7 339
8 340
9 341
10 342
11 343
12 344
13 345
14 346
15 347
16 348
17 349
18 350
19 351
20 352
21 353
22 354
23 355
24 356
25 357
26 358
27 359
28 360
29 361
30 362
31 363
32 364
33 365
34 366
35 367
36 368
37 369
38 370
39 371
40 372
41 373
42 374
43 375
44 376
45 377
46 378
47 379
48 380
49 381
50 382
51 383
52 384
53 385
54 386
55 387
56 388
57 389
58 390
59 391
60 392
of the liquid. Following cell assembly, we checked the integrity of the sealed fluid cell in vacuum, inserted the holder into the electron microscope and allowed it to equilibrate for 20 minutes before imaging.

Bacterial culture growth: Cells of *Magnetospirillum magneticum* AMB-1 (ATCC 700264) used for the *in situ* fluid cell electron holography imaging experiments were grown at room temperature under microaerobic conditions in 5 ml flasks containing the modified flask standard medium (FSM) lacking the major source of iron (ferric citrate) and only containing a small amount of iron (0.36 μ M) present in the mineral solution⁸²⁻⁸⁴. We aimed at using bacterial cells with only freshly formed magnetite magnetosome nanocrystals. The non-magnetic bacterial cultures were then subcultured and FSM medium containing 50 μ M ferric citrate was added to the cells grown under a low iron condition to induce magnetite biomineralization⁸⁴. The microorganisms were sampled 60 minutes after biomineralization induction. They exhibited a somewhat lower number of magnetite nanocrystals, when compared to the use of a regular bacterial growth protocol⁸⁴.

Fluid cell TEM imaging of magnetotactic bacteria: A thin liquid layer containing the specimen was maintained between the SiN windows. As mentioned above, bacterial cells were attached to a (3-Aminopropyl)triethoxysilane (APTES) coated SiN window with a 100 nm SU-8 spacer to render it hydrophilic and positively charged⁵¹, and paired with another 100 nm SU-8 spacer window. Previous low-loss electron energy loss spectroscopy (EELS) revealed that for the used spacer configuration the liquid layer thickness was typically 500–750 nm at the edges and corners of the SiN windows, significantly higher than the nominal thickness of 200 nm⁵¹. The APTES-functionalized window chips encouraged consistent attachment of cells, as described previously⁵¹. The cells were strongly attached and imaged at magnifications of up to 200,000 x without detachment of the bacteria from the SiN window. Preliminary imaging and characterization of the specimens using the fluid cell holder platform was carried out in an FEI Tecnai G² F20 (scanning) TEM operated at an accelerating voltage of 200 kV. This microscope was equipped with a Tridiem Gatan Imaging Filter, a high-angle annular dark-field detector and energy-dispersive X-ray spectroscopy, as reported elsewhere⁵¹.

Off-axis electron holography: Off-axis electron holography experiments were carried out in an FEI Titan 80–300 (scanning) TEM operated at an accelerating voltage of 300 kV. Off-axis electron holograms were acquired in Lorentz mode on a charge-coupled device camera or Gatan K2 direct detection camera using an electron biprism operated at 90–100 V. The experiments were performed at room temperature using magnification ranging from 77,000 \times to 225,000 \times and an acquisition time of 6–8 s. Depending on the magnification of the electron holograms acquired, the Michelson contrast ratios of the reference wave holograms ranged from ~8% to ~30%. Similarly, the average electron count for both 6 and 8 second acquisitions ranged from 1,500 to 10,000 across the magnification range. The estimated dose rate on the specimen is given in Supplementary Material, **Table 1**.

Initial magnetic states and magnetization reversal experiments using the fluid cell: Initial magnetic states were recorded after loading the fluid cell holder into the TEM in close-to-magnetic-field-free conditions. The direction of magnetization of each magnetite nanocrystal chain was subsequently reversed *in situ* in the TEM by tilting the sample by 75° and turning on the conventional microscope objective lens to apply a magnetic field of > 1.5 T parallel to the electron beam direction. The objective lens was then turned off and the sample tilted back to 0° for

1 376
2 377
3 378
4 379
5 379
6 380
7 380
8 381
9 382
10 382
11 383
12
13 384
14
15 385
16 386
17 387
18 388
19 388
20 389
21 390
22 391
23
24 392
25 393
26 394
27
28 395
29 396
30 397
31 398
32
33 399
34
35 400
36 401
37 402
38 403
39
40 404
41
42
43
44
45
46
47
48
49
50
51
52
53
54
55
56
57
58
59
60

hologram acquisition in magnetic-field-free conditions. In this way, holograms were recorded with the chains magnetized in opposite directions. The approach that was used to separate the magnetic from the MIP contribution to the recorded phase shift is described elsewhere⁵⁴. Hence, the subsequent magnetic induction maps present the remanent saturation magnetization of the magnetite chains. For reconstruction of magnetic induction maps, a chosen multiple of the cosine of the magnetic contribution to the phase shift was evaluated to produce magnetic phase contours. Colors were generated from the gradient of the magnetic contribution to the phase shift and added to the contours to show the direction of the projected induction.

Acknowledgments

The present research on *in situ* electron microscopy with a fluid cell was supported by the U.S. Department of Energy, Office of Science, Basic Energy Sciences, Division of Materials Sciences and Engineering. T.P. acknowledges support from a Department of Energy Office of Science Early Career Research Award, Biomolecular Materials Program. The work at Ames Laboratory was supported by the U.S. Department of Energy, Office of Science, Basic Energy Sciences, Division of Materials Science and Engineering. The Ames Laboratory is operated for the U.S. Department of Energy by Iowa State University under contract # DE-AC02-07CH11358. T.P. wishes to thank the laboratory of Dr. Faivre for sharing the bacterial cultures grown under low iron conditions. Off-axis electron holography was carried out in the Ernst Ruska-Centre for Microscopy and Spectroscopy with Electrons in Forschungszentrum Jülich. The research leading to these results received funding from the European Research Council under the European Union's Seventh Framework Programme (FP7/2007-2013)/ ERC grant agreement number 320832. Authors wish to thank Dr. Vadim Migunov for help with the setup and use of Gatan K2 direct detection camera.

Author contributions: T.P. conceived the study. T.P. and T.P.A. designed and carried out the experiments. A.K. assisted with the experimental work and discussions. T.P. and T.P.A. led the writing of the paper, with contributions from A.K and R.E.D-B.

Competing interests: The Authors declare no competing interests.

1
2
3 405
4
5 406
6 407
7 408
8 409
9
10 410
11
12 411
13 412
14 413
15 414
16 415
17 416
18 417
19 418
20 419
21 420
22 421
23 422
24 423
25 424
26 425
27 426
28 427
29 428
30 429
31 430
32 431
33 432
34 433
35 434
36 435
37 436
38 437
39 438
40 439
41 440
42 441
43 442
44 443
45 444
46 445
47 446
48 447
49 448
50 449
51 450
52 451
53 452
54 453
55 454
56 455
57 456
58 457
59 458
60 459

References

- 1 Merla, C. *et al.* Microdosimetry for nanosecond pulsed electric field applications: a parametric study for a single cell. *IEEE transactions on bio-medical engineering* **58**, 1294-1302 (2011).
- 2 Markov, M. XXIst century magnetotherapy. *Electromagnetic biology and medicine* **34**, 190-196 (2015).
- 3 Fröhlich, H. The extraordinary dielectric properties of biological materials and the action of enzymes. *Proc. Nat. Acad. Sci. USA* **72**, 4211-4215 (1975).
- 4 Tuszyn'ski, J. A., Portet, S., Dixon, J. M., Luxford, C. & Cantiello, H. F. Ionic Wave Propagation along Actin Filaments. *Biophys. J.* **86**, 1890-1903 (2004).
- 5 Bazylinski, D. A. & Frankel, R. B. Magnetosome formation in prokaryotes. *Nat Rev Micro* **2**, 217-230, doi:http://www.nature.com/nrmicro/journal/v2/n3/supplinfo/nrmicro842_S1.html (2004).
- 6 Frankel, R. B., Dunin-Borkowski, R. E., Posfai, M. & Bazylinski, D. A. Magnetic microstructure of magnetotactic bacteria. *Handbook of Biomineralization: Biological Aspects and Structure Formation*, 127-144 (2007).
- 7 Lang, C., Schüler, D. & Faivre, D. Synthesis of Magnetite Nanoparticles for Bio- and Nanotechnology: Genetic Engineering and Biomimetics of Bacterial Magnetosomes. *Macromolecular Bioscience* **7**, 144-151, doi:10.1002/mabi.200600235 (2007).
- 8 Budi, A., Legge, F. S., Treutlein, H. & Yarovsky, I. Electric Field Effects on Insulin Chain-B Conformation. *Journal of Physical Chemistry B* **109**, 22641-22648, doi:10.1021/jp052742q (2005).
- 9 Toschi, F., Lugli, F., Biscarini, F. & Zerbetto, F. Effects of Electric Field Stress on a β -Amyloid Peptide. *Journal of Physical Chemistry B* **113**, 369-376, doi:10.1021/jp807896g (2009).
- 10 Xie, Y., Pan, Y., Zhang, R., Liang, Y. & Li, Z. Modulating protein behaviors on responsive surface by external electric fields: A molecular dynamics study. *Applied Surface Science*, Ahead of Print, doi:10.1016/j.apsusc.2014.11.078 (2014).
- 11 Bekard, I. & Dunstan, D. E. Electric field induced changes in protein conformation. *Soft Matter* **10**, 431-437, doi:10.1039/c3sm52653d (2014).
- 12 Beyer, C., Christen, P., Jelesarov, I. & Froehlich, J. Experimental system for real-time assessment of potential changes in protein conformation induced by electromagnetic fields. *Bioelectromagnetics (Hoboken, NJ, United States)* **34**, 419-428, doi:10.1002/bem.21795 (2013).
- 13 Chen, W. Evidence of electroconformational changes in membrane proteins: Field-induced reductions in intra membrane nonlinear charge movement currents. *Bioelectrochemistry* **63**, 333-335, doi:10.1016/j.bioelechem.2003.12.007 (2004).
- 14 Singh, A., Munshi, S. & Raghavan, V. Effect of external electric field stress on gliadin protein conformation. *Proteomes* **1**, 25-39, 15, doi:10.3390/proteomes1020025 (2013).
- 15 Astrakas, L., Gousias, C. & Tzaphlidou, M. Electric field effects on chignolin conformation. *Journal of Applied Physics* **109**, 094702/094701-094702/094705, doi:10.1063/1.3585867 (2011).
- 16 Baker, E. G. *et al.* Local and macroscopic electrostatic interactions in single α -helices. *Nature Chemical Biology* **11**, 221-228, doi:10.1038/nchembio.1739 (2015).
- 17 Kim, S.-Y. Folding and unfolding simulations of a three-stranded beta-sheet protein. *Journal of Materials Science and Chemical Engineering* **4**, 13-17, doi:10.4236/msce.2016.41003 (2016).
- 18 Langer, A., Kaiser, W., Svejda, M., Schwertler, P. & Rant, U. Molecular Dynamics of DNA-Protein Conjugates on Electrified Surfaces: Solutions to the Drift-Diffusion Equation. *Journal of Physical Chemistry B* **118**, 597-607, doi:10.1021/jp410640z (2014).

1 451 19 Beleggia, M. & Zhu, Y. in *Modern Techniques for Characterizing Magnetic Materials*
2 452 (ed Yimei Zhu) 267-326 (Kluwer Academic Publishers 2005).
3 453 20 Formanek, P. *et al.* Electron holography: applications to materials questions. *Annual
4 454 Review of Materials Research* **37**, 539–588 (2007).
5 455 21 Thomas, J. M., Simpson, E. T., Kasama, T. & Dunin-Borkowski, R. E. Electron
6 456 Holography for the Study of Magnetic Nanomaterials. *Acc. Chem. Res.* **41** 665-674 (2008).
7 457 22 Dunin-Borkowski, R. E. *et al.* Off-axis electron holography of exchange-biased
8 458 CoFe/FeMn patterned nanostructures. *J Appl. Phys.* **90**, 2899–2902 (2001).
9 459 23 Kawasaki, T., Endo, J., Matsuda, T., Osakabe, N. & Tonomura, A. Applications of
10 460 holographic interference electron microscopy to the observation of biological specimens. *Journal
11 461 of Electron Microscopy* **35**, 211-214 (1986).
12 462 24 Simon, P. *et al.* Electron holography of biological samples. *Micron* **39**, 229-256,
13 463 doi:10.1016/j.micron.2006.11.012 (2008).
14 464 25 Namiot, V. A. How electron interference can be applied to analyzing the structure of
15 465 small bio-objects and to fast reading of nucleotide sequences. *Biofizika* **53**, 538-543 (2008).
16 466 26 Fink, H. W., Schmid, H., Ermantraut, E. & Schulz, T. Electron holography of individual
17 467 DNA. *J. Opt. Soc. Am. A* **14**, 2168–2172. (1997).
18 468 27 Simon, P., Adhikari, R., Lichte, H., Michler, G. H. & Langela, M. Electron holography
19 469 and AFM studies on styrenic block copolymers and a high impact polystyrene. *J. Appl. Polym.
20 470 Sci.* **96**, 1573–1583 (2005).
21 471 28 Ayache, J., Beaunier, L., Boumendil, J., Ehret, G. & Laub, D. *Sample Preparation
22 472 Handbook for Transmission Electron Microscopy. Methodology.*, (Springer, 2010).
23 473 29 Matsumoto, T. Visualization of DNA in solution by Fraunhofer in-line electron
24 474 holography: I. Simulation. *Optik (Jena, Germany)* **99**, 25-28 (1995).
25 475 30 Simon, P., Lichte, H., Wahl, R., Mertig, M. & Pompe, W. Electron holography of non-
26 476 stained bacterial surface layer proteins. *Biochimica et Biophysica Acta, Biomembranes* **1663**, 178-
27 477 187, doi:10.1016/j.bbamem.2004.03.005 (2004).
28 478 31 Latychevskaia, T., Longchamp, J.-N., Escher, C. & Fink, H.-W. Holography and
29 479 coherent diffraction with low-energy electrons: A route towards structural biology at the single
30 480 molecule level. *Ultramicroscopy* **159**, 395-402, doi:10.1016/j.ultramic.2014.11.024 (2015).
31 481 32 Longchamp, J.-N., Latychevskaia, T., Escher, C. & Fink, H.-W. Low-energy electron
32 482 holographic imaging of individual tobacco mosaic virions. *Applied Physics Letters* **107**,
33 483 133101/133101-133101/133105, doi:10.1063/1.4931607 (2015).
34 484 33 Yu, W., He, X.-l., Liu, C. & Zhu, J.-q. Ptychographic iterative engine with incoherent
35 485 illumination. *Wuli Xuebao* **64**, 244201/244201-244201/244207, doi:10.7498/aps.64.244201
36 486 (2015).
37 487 34 Reinhardt, J. *et al.* Beamstop-based low-background ptychography to image weakly
38 488 scattering objects. *Ultramicroscopy* **173**, 52-57, doi:10.1016/j.ultramic.2016.11.005 (2017).
39 489 35 Hemonnot, C. Y. J. *et al.* X-rays Reveal the Internal Structure of Keratin Bundles in
40 490 Whole Cells. *ACS Nano* **10**, 3553-3561, doi:10.1021/acsnano.5b07871 (2016).
41 491 36 Pan, A., Zhang, X.-f., Wang, B., Zhao, Q. & Shi, Y.-s. Experimental study on three-
42 492 dimensional ptychography for thick sample. *Wuli Xuebao* **65**, 014204/014201-014204/014216,
43 493 doi:10.7498/aps.65.014204 (2016).
44 494 37 Donnelly, C. *et al.* High-resolution hard x-ray magnetic imaging with dichroic
45 495 ptychography. *Physical Review B* **94**, 064421/064421-064421/064429,
46 496 doi:10.1103/PhysRevB.94.064421 (2016).
47 497 38 Rodriguez, J. A., Xu, R., Chen, C.-C., Zou, Y. & Miao, J. Oversampling smoothness: an
48 498 effective algorithm for phase retrieval of noisy diffraction intensities. *Journal of Applied
49 499 Crystallography* **46**, 312-318, doi:10.1107/s0021889813002471 (2013).
50 500

1 500
2 501
3 502
4 503
5 504
6 505
7 506
8 507
9 508
10 509
11 510
12 511
13 512
14 513
15 514
16 515
17 516
18 517
19 518
20 519
21 520
22 521
23 522
24 523
25 524
26 525
27 526
28 527
29 528
30 529
31 530
32 531
33 532
34 533
35 534
36 535
37 536
38 537
39 538
40 539
41 540
42 541
43 542
44 543
45 544
46 545
47 546
48 547
49 548
50 549
51 550
52 551
53 552
54 553
55 554
56 555
57 556
58 557
59 558
60 559

39 Kobayashi, A. *et al.* Specimen preparation for cryogenic coherent X-ray diffraction imaging of biological cells and cellular organelles by using the X-ray free-electron laser at SACLA. *Journal of Synchrotron Radiation* **23**, 975-989, doi:10.1107/s1600577516007736 (2016).

40 Hoyer, P. *et al.* Breaking the diffraction limit of light-sheet fluorescence microscopy by RESOLFT. *Proceedings of the National Academy of Sciences of the United States of America* **113**, 3442-3446, doi:10.1073/pnas.1522292113 (2016).

41 Shibata, N. *et al.* Imaging of built-in electric field at a p-n junction by scanning transmission electron microscopy. *Scientific Reports* **5**, 10040, doi:10.1038/srep10040 (2015).

42 Majert, S. & Kohl, H. High-resolution STEM imaging with a quadrant detector-Conditions for differential phase contrast microscopy in the weak phase object approximation. *Ultramicroscopy* **148**, 81-86, doi:10.1016/j.ultramic.2014.09.009 (2015).

43 Denneulin, T., Houdellier, F. & Hytch, M. Differential phase-contrast dark-field electron holography for strain mapping. *Ultramicroscopy* **160**, 98-109, doi:10.1016/j.ultramic.2015.10.002 (2016).

44 de Jonge, N. & Ross, F. M. Electron microscopy of specimens in liquid. *Nature Nanotechnology* **6**, 695-704, doi:10.1038/nnano.2011.161 (2011).

45 Peckys, D. B., Dukes, M. J., Ring, E. A., Piston, D. W. & de Jonge, N. Imaging specific protein labels on eukaryotic cells in liquid with scanning transmission electron microscopy. *Microscopy Today* **19**, 16, 18-20, doi:10.1017/s1551929511000903 (2011).

46 Peckys, D. B. & de Jonge, N. Liquid Scanning Transmission Electron Microscopy: Imaging Protein Complexes in their Native Environment in Whole Eukaryotic Cells. *Microscopy and Microanalysis* **20**, 346-365, doi:10.1017/s1431927614000099 (2014).

47 Kashyap, S., Woehl, T. J., Liu, X., Mallapragada, S. K. & Prozorov, T. Nucleation of Iron Oxide Nanoparticles Mediated by Mms6 Protein In Situ. *ACS Nano* **8**, 9097-9106, doi:<http://dx.doi.org/10.1021/nn502551y> (2014).

48 Wang, C., Qiao, Q., Shokuhfar, T. & Klie, R. F. High-Resolution Electron Microscopy and Spectroscopy of Ferritin in Biocompatible Graphene Liquid Cells and Graphene Sandwiches. *Advanced Materials (Weinheim, Germany)* **26**, 3410-3414, doi:10.1002/adma.201306069 (2014).

49 Dukes, M. J., Ramachandra, R., Baudoin, J.-P., Gray Jerome, W. & de Jonge, N. Three-dimensional locations of gold-labeled proteins in a whole mount eukaryotic cell obtained with 3 nm precision using aberration-corrected scanning transmission electron microscopy. *Journal of Structural Biology* **174**, 552-562, doi:10.1016/j.jsb.2011.03.013 (2011).

50 Dukes, M. J. *Scanning transmission electron microscopy of tagged proteins in whole eukaryotic cells*, (2011).

51 Woehl, T. J. *et al.* Correlative Electron and Fluorescence Microscopy of Magnetotactic Bacteria in Liquid: Toward In Vivo Imaging. *Scientific Reports*, **4**, 6854, doi:10.1038/srep06854 (2014).

52 Woehl, T. J. & Prozorov, T. in *Liquid Cell Electron Microscopy* (eds Frances Ross & Niels de Jonge) Ch. 23, 476-500 (Cambridge University Press, 2017).

53 Shirai, M. *et al.* In situ electron holographic study of Ionic liquid. *Ultramicroscopy* **146**, 125-129, doi:10.1016/j.ultramic.2014.08.003 (2014).

54 Dunin-Borkowski, R. E. *et al.* Magnetic microstructure of magnetotactic bacteria by electron holography. *Science* **282**, 1868-1870 (1998).

55 Dunin-Borkowski, R. E. *et al.* Off-axis electron holography of magnetotactic bacteria: magnetic microstructure of strains MV-1 and MS-1. *Eur. J. Mineral.* **13**, 671–684 (2001).

56 Simpson, E. T. *et al.* Magnetic induction mapping of magnetite chains in magnetotactic bacteria at room temperature and close to the Verwey transition using electron holography. *Journal of Physics: Conference Series* **17**, 108-121, doi:10.1088/1742-6596/17/1/017 (2005).

1 548
2 549
3 549
4 550
5 551
6 552
7 553
8 554
9 554
10 555
11 556
12 557
13 558
14 559
15 559
16 560
17 561
18 562
19 563
20 564
21 565
22 565
23 566
24 567
25 568
26 569
27 570
28 571
29 571
30 572
31 573
32 574
33 575
34 575
35 576
36 577
37 578
38 579
39 580
40 581
41 581
42 582
43 583
44 584
45 585
46 586
47 587
48 587
49 588
50 589
51 590
52 591
53 592
54 592
55 593
56 594
57 595
58
59
60

57 Staniland, S., Ward, B., Harrison, A., van der Laan, G. & Telling, N. Rapid magnetosome formation shown by real-time x-ray magnetic circular dichroism. *Proc. Natl. Acad. Sci.* **104**, 19524-19528, doi:10.1073/pnas.0704879104 (2007).

58 Fdez-Gubieda, M. L. *et al.* Magnetite biominerization in Magnetospirillum gryphiswaldense: time-resolved magnetic and structural studies. *ACS Nano* **7**, 3297-3305, doi:10.1021/nn3059983 (2013).

59 Zhu, X. H. *et al.* in *AIP Conference Proceedings [0094-243X]*. 020002 (American Institute of Physics).

60 Midgley, P. A. & Dunin-Borkowski, R. E. Electron tomography and holography in materials science. *Nat. Mater.* **8**, 271-280, doi:doi: 10.1038/nmat2406 (2009).

61 Devouard, B. *et al.* Magnetic from magnetotactic bacteria: size distributions and twinning. *American Mineralogist* **83**, 1387-1398 (1998).

62 Kasama, T., Dunin-Borkowski, R. E. & Beleggia, M. in *Holography—Different Fields of Application* (ed F. A. Monroy Ramírez) 53-80 (InTech, 2011).

63 Grogan, J. M., Schneider, N. M., Ross, F. M. & Bau, H. H. Bubble and Pattern Formation in Liquid Induced by an Electron Beam. *Nano Letters* **14**, 359-364, doi:10.1021/nl404169a (2014).

64 Schneider, N. M. *et al.* Electron-Water Interactions and Implications for Liquid Cell Electron Microscopy. *Journal of Physical Chemistry C* **118**, 22373-22382, doi:10.1021/jp507400n (2014).

65 Mirsaidov, U., Ohl, C.-D. & Matsudaira, P. A direct observation of nanometer-size void dynamics in an ultra-thin water film. *Soft Matter* **8**, 7108-7111, doi:10.1039/c2sm25331c (2012).

66 Komeili, A., Vali, H., Beveridge, T. J. & Newman, D. K. Magnetosome vesicles are present before magnetite formation, and MamA is required for their activation. *P. Natl. Acad. Sci. USA* **101**, 3839-3844 (2004).

67 Lang, C. & Schueler, D. Biogenic nanoparticles: production, characterization, and application of bacterial magnetosomes. *Journal of Physics: Condensed Matter* **18**, S2815-S2828 (2006).

68 Schueler, D. Nano crystals for magnetic field orientation. Biominerization of magnetosomes in bacteria. *BIOspektrum* **11**, 291-294 (2005).

69 Matsunaga, T., Sakaguchi, T. & Tadokoro, F. Magnetite formation by a magnetic bacterium capable of growing aerobically. *Applied Microbiology and Biotechnology* **35**, 651-655, doi:10.1007/bf00169632 (1991).

70 Bazylinski, D. A. & Frankel, R. B. Magnetic iron oxide and iron sulfide minerals within microorganisms: Potential biomarkers. *Biominerization (2nd Edition)*, 17-43 (2004).

71 Prozorov, R. *et al.* Magnetic irreversibility and Verwey transition in nano-crystalline bacterial magnetite. *Phys. Rev. B. Cond. Mat.* **76**, 054406 054401-054410 (2007).

72 Scheffel, A. *et al.* An acidic protein aligns magnetosomes along a filamentous structure in magnetotactic bacteria. *Nature* **440**, 110-114 (2005).

73 Komeili, A., Li, Z., Newman, D. K. & Jensen, G. J. Magnetosomes are cell membrane invaginations organized by the actin-like protein MamK. *Science* **311**, 242-245 (2006).

74 McCartney, M. R., Lins, U., Farina, M., Buseck, P. R. & Frankel, R. B. Magnetic microstructure of bacterial magnetite by electron holography. *Eur. J. Mineral.* **13**, 685-689, doi:10.1127/0935-1221/2001/0013-0685 (2001).

75 Posfai, M., Kasama, T. & Dunin-Borkowski, R. E. Biominerals at the nanoscale: transmission electron microscopy methods for studying the special properties of biominerals. *EMU Notes in Mineralogy* **14**, 375-433 (2013).

76 Sellner, B. & Kathmann, S. M. A matter of quantum voltages. *Journal of Chemical Physics* **141**, 18C534/531-518C534/513, doi:10.1063/1.4898797 (2014).

1 596
2 597
3 598
4 599
5 600
6 601
7 602
8 603
9 604
10 605
11 606
12 607
13 608
14 609
15 610
16 611
17 612
18 613
19 614
20 615
21 616
22 617
23 618
24 619
25 620
26 621
27 622
28 623
29 624
30 625
31 626
32 627
33 628
34 629
35 630
36 631
37 632
38 633
39 634
40 635
41 636
42 637
43 638
44 639
45 640
46 641
47 642
48 643
49 644
50 645
51 646
52 647
53 648
54 649
55 650
56 651
57 652
58 653
59 654
60 655

77 Kathmann, S. M., Kuo, I. F. W. & Mundy, C. J. Electronic Effects on the Surface Potential at the Vapor-Liquid Interface of Water. *Journal of the American Chemical Society* **130**, 16556-16561, doi:10.1021/ja802851w (2008).

78 Kathmann, S. M., Kuo, I. F. W., Mundy, C. J. & Schenter, G. K. Understanding the surface potential of water. *Journal of Physical Chemistry B* **115**, 4369-4377, doi:10.1021/jp1116036 (2011).

79 Kathmann, S. M., Sellner, B., Alexander, A. J. & Valiev, M. Beyond classical theories. *AIP Conference Proceedings* **1527**, 109-112, doi:10.1063/1.4803215 (2013).

80 Harscher, A. & Lichte, H. in *ICEM14*. (eds H.A. Calderon Benavides & M. J. Yacaman) 553-554 (Institute of Physics Publishing, 1998).

81 Simon, P. *et al.* Electron holography of organic and biological materials. *Advanced Materials (Weinheim, Germany)* **15**, 1475-1481, doi:10.1002/adma.200301645 (2003).

82 Heyen, U. & Schüler, D. Growth and magnetosome formation by microaerophilic Magnetospirillum strains in an oxygen-controlled fermentor. *Appl Microbiol Biotechnol* **61**, 536-544, doi:10.1007/s00253-002-1219-x (2003).

83 Faivre, D., Menguy, N., Posfai, M. & Schüler, D. Environmental parameters affect the physical properties of fast-growing magnetosomes. *American Mineralogist* **93**, 463-469, doi:10.2138/am.2008.2678 (2008).

84 Firlar, E., Perez Gonzalez, T., Olszewska, A., Faivre, D. & Prozorov, T. Following Iron Speciation in the Early Stages of Magnetite Magnetosome Biomineralization. *J. Mater. Res. Focus issue on Biomineralization and Biomimetics* **31**, 547-555 (2016).

1 Figure Legends

2 619
3
4 620
5 621
6 622
7
8 623
9 624
10
11 625
12
13 626
14 627
15 628
16
17 629
18 630
19 631
20 632
21
22 633
23 634
24 635
25 636
26
27 637
28 638
29 639
30
31 640
32 641
33 642
34 643
35
36
37 644
38 645
39 646
40
41 647
42 648
43 649
44
45 650
46 651
47
48 652
49 653
50
51 654
52 655
53 656
54
55 657
56 658
57 659
58 660
59
60

Figure 1. Schematic diagrams showing the experimental setup in the present study. (A) TEM imaging with a fluid cell (not to scale). The microfluidic chamber consists of two silicon microchips supporting two 50-nm-thick electron-transparent SiN membranes. Cells of *M. Magneticum* are attached to the top SiN window and imaged using an incident electron beam in a thin liquid layer. (B) Off-axis electron holography using a fluid cell (adapted from ⁶⁰).

Figure 2. Electron holography and associated analysis of a hydrated bacterial cell. (A) Off-axis electron hologram of a hydrated bacterial cell between two SiN membranes. The scale bar is 200 nm. The magnified region in the inset shows well-resolved interference fringes with a spacing of \sim 5.6 nm. (B) Wrapped phase image showing a $0 - 2\pi$ range of phase values presented in the image and (C) amplitude image of the bacterial cell in (A). (D-F) Off-axis electron holograms acquired in (D) the initial state, (E) after tilting by $+75^\circ$ and applying a magnetic field in the electron beam direction and (F) after tilting by -75° and applying a magnetic field in the electron beam direction. The scale bars are 100 nm. The spacing of the holographic interference fringes is \sim 5.7 nm. Examples of electron-beam-induced changes to the specimen include the progression of voids outlined in yellow and red. (G) Magnetic induction map of the magnetite chain in the bacterial cell reconstructed from the dashed area in (F). The black phase contours were formed from the magnetic contribution to the recorded phase shift and have a spacing of 0.098 ± 0.001 radians. The outlines of the individual magnetite nanocrystals are marked in white. The direction of the measured projected in-plane magnetic induction is shown using arrows and colors, according to the color wheel shown in the inset. The in-plane component of the magnetic field applied to the specimen before recording the holograms in (E) and (F) is labelled FD and marked by blue and red arrows. (H) Profile of the magnetic contribution to the phase shift across the magnetite particle shown in (G) denoted by a red dashed line, yielding a saturation magnetic induction of 0.58 ± 0.1 T.

Figure 3. Electron holography and visualized magnetization of a magnetite nanocrystal chain. (A) Off-axis electron hologram of a magnetite nanocrystal chain that had been released from a ruptured bacterium, showing well-resolved holographic interference fringes with a spacing of \sim 6.2 nm. The scale bar is 100 nm. (B) Corresponding magnetic induction map. The phase contour spacing is 0.31 ± 0.001 radians. The in-plane component of the magnetic field applied to the specimen before recording the holograms is labelled FD and marked by blue and red arrows. (C) Profile of the magnetic contribution to the phase shift across the magnetite particle shown in (B) denoted by a red dashed line, yielding a saturation magnetic induction of 0.63 ± 0.1 T.

Figure 4. Electron holography and associated analysis of regions of liquid. (A, B) Off-axis electron holograms recorded from the middle of the fluid cell and from a liquid front that partially covers the SiN window, respectively. The scale bars are 200 nm in (A) and 300 nm in (B). The magnified regions in the insets show well-resolved interference fringes with a spacing of \sim 6.2 nm. (C) Off-axis electron hologram recorded from a droplet of liquid in the fluid cell (\sim 1200 nm in diameter and assumed to be \sim 800 nm in height) with a holographic interference fringe spacing of \sim 5.7 nm. The scale bar is 200 nm. (D) Radial average of intensity of the droplet shown in (C). (E) Amplitude image, (F) t/λ profile across the droplet, and (G) phase profile across the droplet reconstructed using off-axis electron holography. The scale bar in (E) is 200 nm.

1 661
2 662
3 663
4 664
5 665
6 666
7 667
8 668
9 669
10 670
11 671
12 672
13 673
14 674
15 675
16 676
17 677
18 678
19 679
20 680
21 681
22 682
23 683
24 684
25 685
26 686
27 687
28 688
29 689
30 690
31 691
32 692
33 693
34 694
35 695
36 696
37 697
38 698
39 699
40 700
41 701
42 702
43 703
44 704
45 705
46 706
47 707
48 708
49 709
50 710
51 711
52 712
53 713
54 714
55 715
56 716
57 717
58 718
59 719
60 720

Figure 5. Comparison of off-axis electron holograms recorded using two cameras. Off-axis electron holograms recorded from the fluid cell using (A) a conventional CCD camera and (B) a K2 direct electron detector. A 6 s acquisition time was used in each case.

For Review Only

1 692
2
3
4
5
6
7
8
9
10
11
12
13
14
15
16
17
18
19
20
21
22
23
24
25
26
27
28
29
30
31
32
33
34
35
36
37
38
39
40
41
42
43
44
45
46
47
48
49
50
51
52
53
54
55
56
57
58
59
60

For Review Only

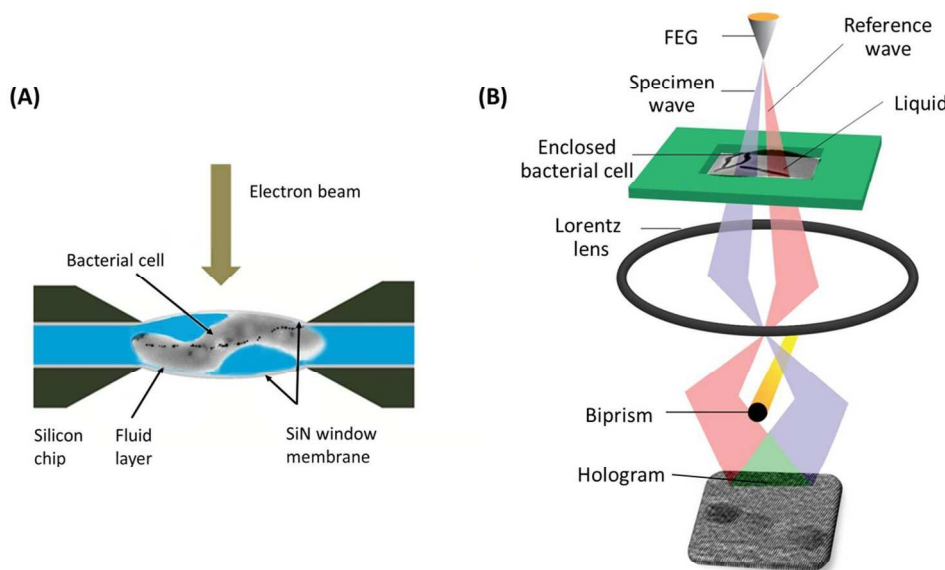


Figure 1. Schematic diagrams showing the experimental setup in the present study. (A) TEM imaging with a fluid cell (not to scale). The microfluidic chamber consists of two silicon microchips supporting two 50-nm-thick electron-transparent SiN membranes. Cells of *M. Magneticum* are attached to the top SiN window and imaged using an incident electron beam in a thin liquid layer. (B) Off-axis electron holography using a fluid cell (adapted from 60).

254x168mm (150 x 150 DPI)

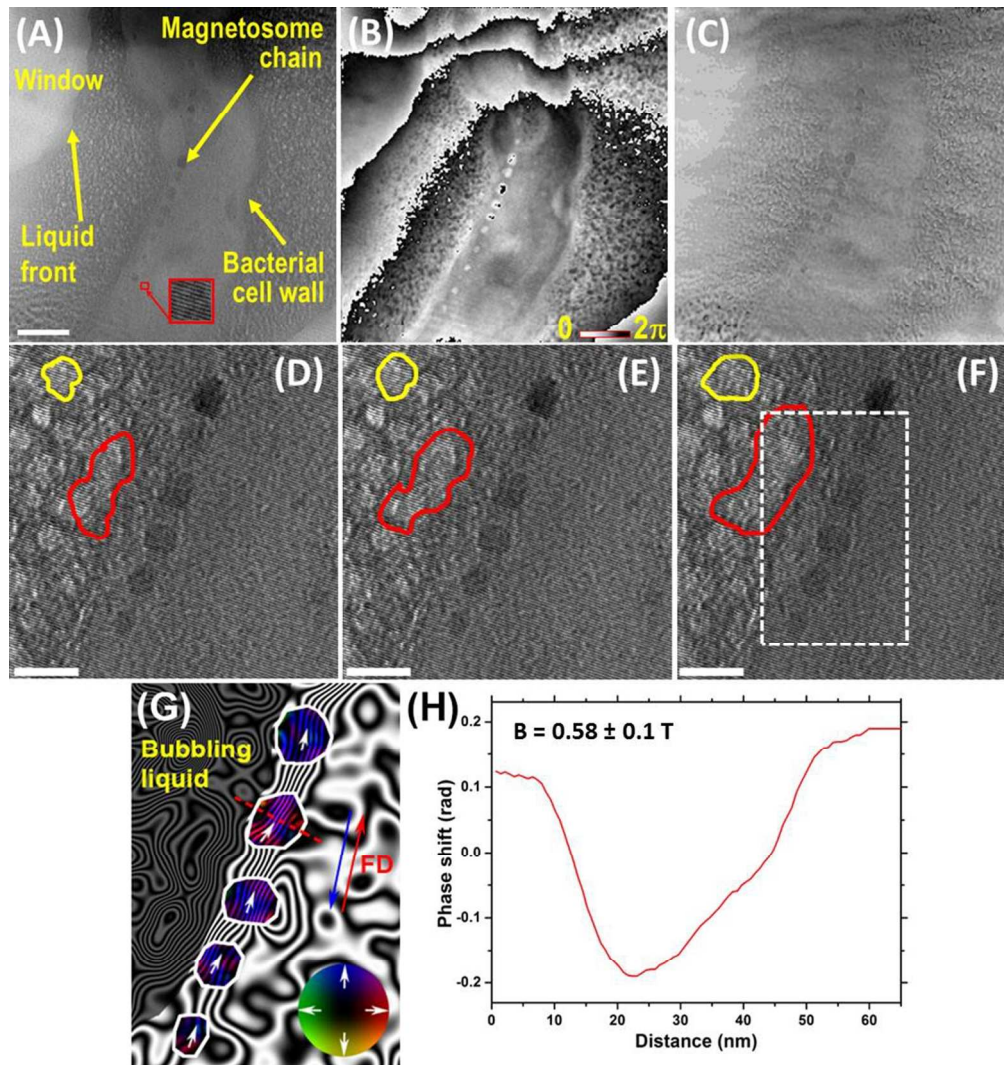


Figure 2. Electron holography and associated analysis of a hydrated bacterial cell. (A) Off-axis electron hologram of a hydrated bacterial cell between two SiN membranes. The scale bar is 200 nm. The magnified region in the inset shows well-resolved interference fringes with a spacing of ~ 5.6 nm. (B) Wrapped phase image showing a $0 - 2\pi$ range of phase values presented in the image and (C) amplitude image of the bacterial cell in (A). (D-F) Off-axis electron holograms acquired in (D) the initial state, (E) after tilting by $+75^\circ$ and applying a magnetic field in the electron beam direction and (F) after tilting by -75° and applying a magnetic field in the electron beam direction. The scale bars are 100 nm. The spacing of the holographic interference fringes is ~ 5.7 nm. Examples of electron-beam-induced changes to the specimen include the progression of voids outlined in yellow and red. (G) Magnetic induction map of the magnetite chain in the bacterial cell reconstructed from the dashed area in (F). The black phase contours were formed from the magnetic contribution to the recorded phase shift and have a spacing of 0.098 ± 0.001 radians. The outlines of the individual magnetite nanocrystals are marked in white. The direction of the measured projected in-plane magnetic induction is shown using arrows and colors, according to the color wheel shown in the inset. The in-plane component of the magnetic field applied to the specimen before recording the holograms in (E) and (F) is labelled FD and marked by blue and red arrows. (H) Profile of the magnetic contribution to the phase shift across the magnetite particle shown in (G) denoted by a red dashed line, yielding a saturation magnetic induction of 0.58 ± 0.1 T.

180x190mm (150 x 150 DPI)

For Review Only

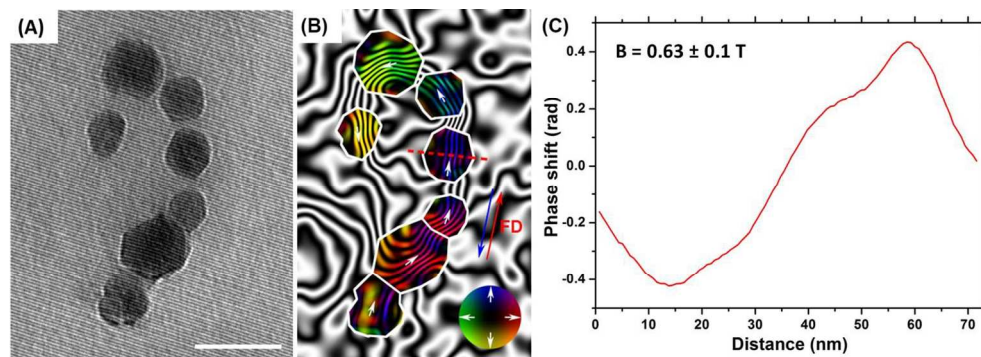


Figure 3. Electron holography and visualized magnetization of a magnetite nanocrystal chain. (A) Off-axis electron hologram of a magnetite nanocrystal chain that had been released from a ruptured bacterium, showing well-resolved holographic interference fringes with a spacing of ~ 6.2 nm. The scale bar is 100 nm. (B) Corresponding magnetic induction map. The phase contour spacing is 0.31 ± 0.001 radians. The in-plane component of the magnetic field applied to the specimen before recording the holograms is labelled FD and marked by blue and red arrows. (C) Profile of the magnetic contribution to the phase shift across the magnetite particle shown in (B) denoted by a red dashed line, yielding a saturation magnetic induction of 0.63 ± 0.1 T.

254x89mm (150 x 150 DPI)

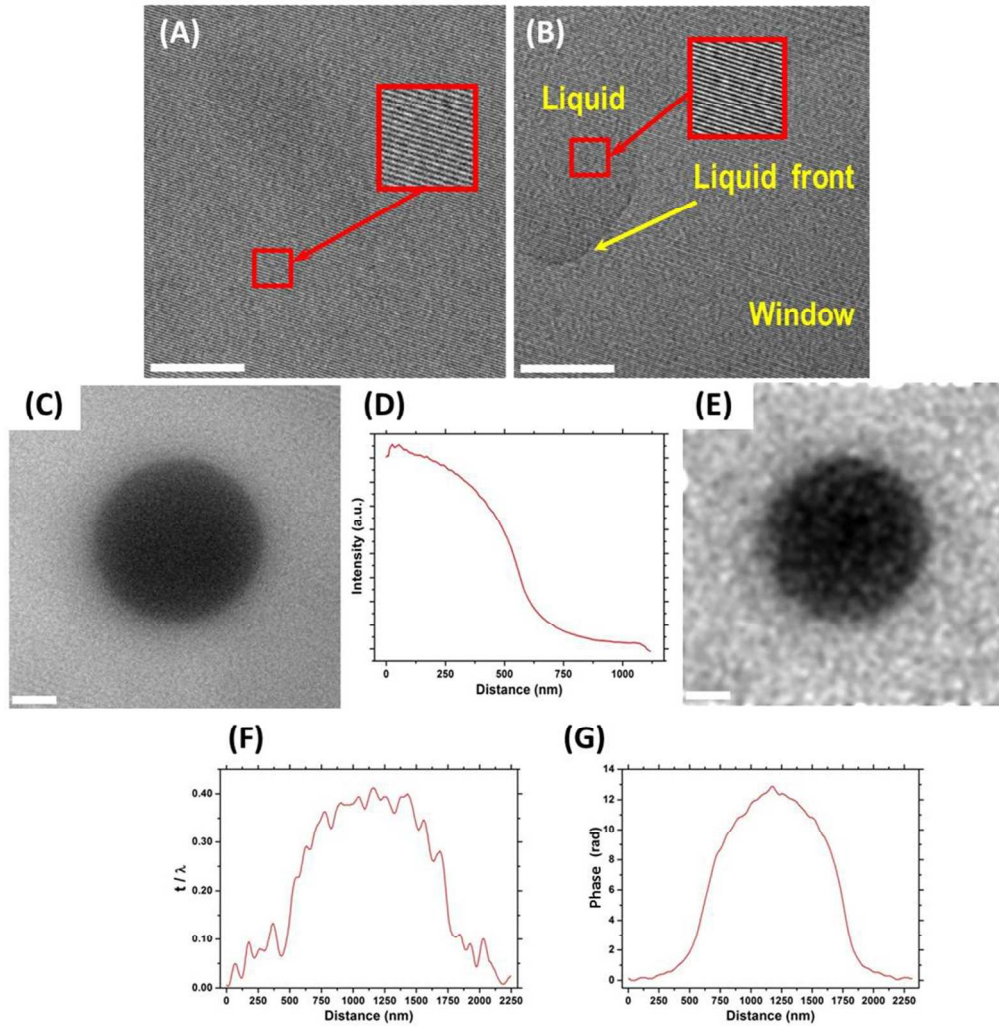


Figure 4. Electron holography and associated analysis of regions of liquid. (A, B) Off-axis electron holograms recorded from the middle of the fluid cell and from a liquid front that partially covers the SiN window, respectively. The scale bars are 200 nm in (A) and 300 nm in (B). The magnified regions in the insets show well-resolved interference fringes with a spacing of ~ 6.2 nm. (C) Off-axis electron hologram recorded from a droplet of liquid in the fluid cell (~ 1200 nm in diameter and assumed to be ~ 800 nm in height) with a holographic interference fringe spacing of ~ 5.7 nm. The scale bar is 200 nm. (D) Radial average of intensity of the droplet shown in (C). (E) Amplitude image, (F) t/λ profile across the droplet, and (G) phase profile across the droplet reconstructed using off-axis electron holography. The scale bar in (E) is 200 nm.

183x190mm (150 x 150 DPI)

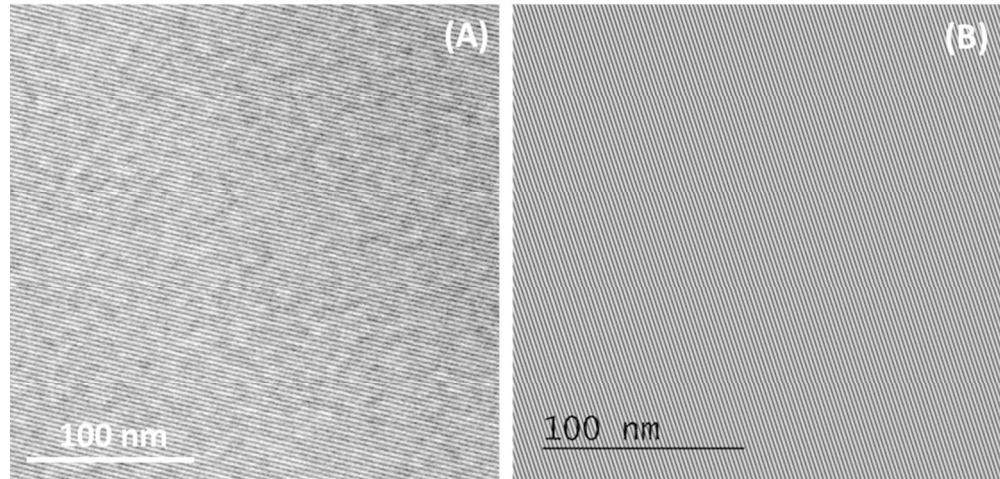


Figure 5. Comparison of off-axis electron holograms recorded using two cameras. Off-axis electron holograms recorded from the fluid cell using (A) a conventional CCD camera and (B) a K2 direct electron detector. A 6 s acquisition time was used in each case.

189x90mm (150 x 150 DPI)